

Laser-rf creation and diagnostics of seeded atmospheric pressure air and nitrogen plasmas

Siqi Luo,^{a)} C. Mark Denning, and John E. Scharer

Electrical and Computer Engineering, University of Wisconsin—Madison, Madison, Wisconsin 53705, USA

(Received 27 July 2007; accepted 18 April 2008; published online 2 July 2008)

A laser initiation and radio frequency (rf) sustainment technique has been developed and improved from our previous work to create and sustain large-volume, high-pressure air and nitrogen plasmas. This technique utilizes a laser-initiated, 15 mTorr partial pressure tetrakis (dimethylamino) ethylene seed plasma with a 75 Torr background gas pressure to achieve high-pressure air/nitrogen plasma breakdown and reduce the rf power requirement needed to sustain the plasma. Upon the laser plasma initiation, the chamber pressure is raised to 760 Torr in 0.5 s through a pulsed gas valve, and the end of the chamber is subsequently opened to the ambient air. The atmospheric-pressure plasma is then maintained with the 13.56 MHz rf power. Using this technique, large-volume (1000 cm³), high electron density (on the order of 10^{11–12} cm⁻³), 760 Torr air and nitrogen plasmas have been created while rf power reflection is minimized during the entire plasma pulse utilizing a dynamic matching method. This plasma can project far away from the antenna region (30 cm), and the rf power budget is 5 W/cm³. Temporal evolution of the plasma electron density and total electron-neutral collision frequency during the pulsed plasma is diagnosed using millimeter wave interferometry. Optical emission spectroscopy (OES) aided by SPECAIR, a special OES simulation program for air-constituent plasmas, is used to analyze the radiating species and thermodynamic characteristics of the plasma. Rotational and vibrational temperatures of 4400–4600 ± 100 K are obtained from the emission spectra from the N₂(2+) and N₂⁺(1-) transitions by matching the experimental spectrum results with the SPECAIR simulation results. Based on the relation between the electron collision frequency and the neutral density, utilizing millimeter wave interferometry, the electron temperature of the 760 Torr nitrogen plasma is found to be 8700 ± 100 K (0.75 ± 0.1 eV). Therefore, the plasma deviates significantly from local thermal equilibrium. © 2008 American Institute of Physics. [DOI: 10.1063/1.2946718]

I. INTRODUCTION

The efficient creation of large-volume, atmospheric-pressure, air-constituent plasmas allows a variety of application possibilities in the fields of material processing and device fabrication,¹ biological decontamination, environmental processing of noxious gases, medical sterilization,² and drag and radar cross-section reduction of aircraft.^{3–6}

A. The power budget of atmospheric-pressure air plasmas

The kinetics of reactions and transitions in atmospheric-pressure air or nitrogen plasmas is a very complex topic that has been thoroughly studied by a number of researchers.^{7,8} A much higher rf power density is required to initiate atmospheric-pressure air or nitrogen plasmas compared to low pressure (<1 Torr) plasmas. Here we give an overview of the primary reasons for the very high power requirement for creation of atmospheric-pressure air plasmas. In atmospheric-pressure plasmas, the energetic free electrons, once created, will collide with heavy particles including neutrals and ions with a very high collision frequency (10¹¹ Hz as diagnosed by millimeter wave interferometry), lose their kinetic energy, and subsequently recombine with ions or at-

tach to neutral species on a much faster time scale than in low pressure (<1 Torr) plasmas. Electron-neutral collision is the dominant collision process in our low-fractional-ionization atmospheric plasmas. In high-pressure air and nitrogen plasmas, the excited metastable states, especially the vibrational states, are closely coupled with the free electron energies. Therefore, the electric field energy transferred to the free electrons will also excite molecular vibrational states on a very fast time scale.^{8–11} Additionally, the two-body and three-body electronic recombination and attachment rates of air and nitrogen plasma species including O₂⁺, O₂, and N₂⁺ are also very high.¹² The resonant rotational and vibrational states of air molecules store kinetic energy from electron collisions and dissipate a significant amount of the energy through radiative transitions. The collisional power loss through the Pyrex® chamber to the ambient air in the form of heat is also considerable because the neutral gas temperature of the plasma is found to be 4400 ± 50 K from optical emission spectroscopy (OES), giving rise to a very high heat flux. As a result of these various processes, free electron energy levels in atmospheric-pressure air and nitrogen plasmas are on the order of 1–3 eV, and hence the ionization efficiency is generally low (less than 0.1%), while the deionization processes including recombination and attachment are very efficient. Therefore, very high power budgets are required to accelerate electrons to sufficiently high kinetic

^{a)}Electronic mail: siqi.luo@gmail.com.

energies in order to ionize neutrals and initiate a large-volume atmospheric plasma discharge if only radio frequency power is utilized to ionize the atmospheric discharge and if no external electron sources are used to assist ionization. By the theoretical approximation of Adamovich *et al.*,⁹ 30 kW/cm³ dc or rf electric power density is generally required to sustain an electron density $n_e \geq 10^{13}$ cm⁻³ when the neutral gas temperature is 2000 K. Therefore, in general, low ionization efficiency and fast attachment and recombination rates are the causes of a high power budget. While these loss processes remain the same whether one is initiating or sustaining a discharge, the mechanism for ionization which balances against these losses (rf coupling to electrons and their subsequent ionizing collisions with neutral particles) is strongly affected by the initial density of electrons. We have observed that without laser preionization, a much higher rf power is required for plasma initiation due to a much lower population of electrons to couple rf power to, compared to sustaining an already existing discharge. In some cases (higher pressures) it is not possible to initiate the plasma with rf alone. Additionally, studies by various researchers^{7,9,13,14} also point to the fact that having a pre-existing high-density plasma and/or high-energy electrons greatly reduces the initiating power budget by increasing the ionization efficiency.

In view of this high power budget challenge, both computational and experimental research has been conducted by various researchers to make stable high-pressure air plasmas more power efficient. These efforts involve two main tactics: improvement of the ionization efficiency by the means of external electron sources or strong local electric fields^{7,13} and control of deionization processes such as attachment and recombination by CO laser optical pumping or preheating the gas to 2000 K.^{9,15}

In order to improve the ionization efficiency, Macheret *et al.*¹³ and Adamovich *et al.*^{9,15} studied the plasmas generated by high-energy electron beams. Because the electron beams have very high energies (on the order of 100 keV)⁷ and high ionization efficiencies (40%–50%), a power budget as low as 30 W/cm³ was achieved.¹³ In an alternative scheme studied by Macheret *et al.*¹³ and Kruger *et al.*¹⁶ to increase ionization efficiency, a strong local electric field was applied *in situ* to produce high-energy electrons. To sustain the average n_e at above 10^{12} cm⁻³ for extended periods while minimizing the power budget, this electric field is applied for only a short time (tens of nanoseconds) to raise n_e to 10^{13} cm⁻³, and the plasma is allowed to decay over microseconds to 10^{12} cm⁻³ level. The electric field pulse is repeated, therefore sustaining the plasma at a desired n_e level. In this scheme, a time-average power budget of 100 W/cm³ is required to sustain a 10^{13} cm⁻³ electron density and about ten times less to sustain at 10^{12} cm⁻³ with plasma volumes on the order of 1 cm³.

The lowest electric power budget was achieved by preheating the gas to 2000 K prior to the repetitively pulsed electric field ionization.¹⁶ Preheating the gas assists reduction of the power budget because at elevated neutral gas temperatures, the electron attachment rate to oxygen is effectively reduced. As a result, two-body dissociative electron-ion re-

combination replaces the electron attachment to oxygen as the primary deionization process.⁷ In Kruger's experiment, only 12 W/cm³ was required to sustain a time-averaged n_e of 10^{12} cm⁻³ with gas preheating to 2000 K. The plasma volumes were on the order of 1 cm³. This experimental result agrees well with the authors' two-temperature kinetic model that predicts a 9 W/cm³ power budget.¹⁶ It should be noted that the heating of the gas consumes a significant amount of power that also needs to be accounted for when determining the total power budget for plasma sustainment.⁷ A different method modifies electron removal rates by CO laser optical pumping to control metastable species concentrations and excited state populations in the plasma.^{7,9,15} This method was effective in reducing the power budget to 45 W/cm³ (Refs. 9 and 15) and creates plasmas with electron densities of 8×10^{11} and volumes on the order of 1 cm³.

B. Overview of the laser-initiated and rf-sustained plasma technique

In our experiment, in order to create a power-efficient, large-volume atmospheric plasma, breakdown of atmospheric-pressure air is assisted by a laser-produced seed plasma. This seeded plasma can be produced with a low sustaining rf power density of 5 W/cm³ and a rapid formation time ($t < 0.5$ s).

The use of a laser-initiated tetrakis (dimethylamino) ethylene (TMAE) plasma greatly assists plasma formation and reduces the rf power requirements. The excimer laser at 193 nm has photon energy of 6.4 eV, which can readily ionize TMAE (ionization potential of 6.1 eV) through a single-photon ionization process. This laser-produced plasma has been examined in our group's previous work by Ding,¹⁷ Kelly,¹⁸ and Akhtar.¹² The 20 ns laser pulse energy is typically 100 mJ with a beam cross section of 2.8 cm \times 1.2 cm², resulting in a flux of 1.5 MW/cm² that readily produces a high-density ($n_e \approx 10^{14}$ cm⁻³) laser-produced plasma. This UV laser-produced plasma acts as an effective seed plasma allowing relatively low rf power levels to propagate within, sustain, and enlarge the plasma to create a large-volume steady-state discharge at 760 Torr. Alternatively, a relatively low cost set of UV flash tubes and focusing mirrors with smaller weight and volume could provide the seed plasma in place of the ArF UV laser that we used to focus on the physical processes of the technique. The rf-sustained plasmas are projected as far as 30 cm from the helical antenna at atmospheric pressure due to the 60-cm-long initially created laser seed plasma.

We have shown in our previously published work¹⁹ that the plasma load impedance as seen at the input of the helical antenna varies significantly from the vacuum helical antenna impedance during the 2 ms fast-pulsed rf plasma formation following the initiating laser pulse. This variation in plasma load impedance presents a challenge to the rf generator and matching system. Based on the previous work, in order to ensure efficient rf power coupling to the plasma, a new dynamic rf measurement and matching system has been designed and implemented. A dual directional coupler and two rf detectors are used to precisely measure the incident and

reflected rf power level at the input of the matchbox. A circuit compares the incident and reflected rf powers, using the transient in the rf power reflection coefficient due to the plasma load impedance variation as a switching trigger. The transient signal is detected and amplified by the comparator circuit that is used to switch the matching network on a short time scale (4 ms) to compensate for the plasma loaded helical antenna impedance variation. Using this method, rf power reflections are minimized during the entire rf pulse.

Two primary diagnostics are performed on the high-pressure, laser-initiated, rf-sustained air and nitrogen plasmas: millimeter wave interferometry and optical emission spectroscopy. Millimeter wave interferometry is used to diagnose the electron density n_e and the total electron collision frequency ν (often simply referred to as the electron collision frequency) of the plasma. Because the ionization fraction is very low in atmospheric-pressure plasmas, ν is approximately equal to the electron-neutral collision frequency ν_{en} . This diagnostic is based on the property that the millimeter wave propagates in an unmagnetized plasma with a reduced phase constant β_p and an increased attenuation constant α_p compared to the free space values β_0 and α_0 . This is because the plasmas typically have a complex Lorentz conductivity and, therefore, a complex Lorentz dielectric constant which is a function of n_e and ν (discussed in detail in Sec. II).²⁰ Millimeter wave interferometry measures the change in β_p and α_p , enabling the computation of the electron density and the electron collision frequency from the measured data.

Plasma OES is used to diagnose the emitting species and thermodynamic behavior of the plasmas. The presence of characteristic lines in the plasma emission spectra can be used to identify the existence of certain excited states of the species in the plasma. The profiles and emission intensity ratios of certain characteristic lines can be used to obtain the rotational and vibrational temperatures of the associated species. This is done by matching the experimental spectrum results with the SPECAIR code-simulated results.^{8,11,21} For this purpose, emission spectra from such transitions as the N₂ C-B (2+) and N₂⁺ B-X (1-) are especially useful.

Based on the collision frequency measured from millimeter wave interferometry and the translational neutral gas temperature (T_{trans}) obtained from OES, the electron temperature T_e can be determined. This method was first developed and implemented in our previous work¹⁸ with assumed neutral heating rates for the 760 Torr argon and 75 Torr nitrogen plasmas. In this new work, it is accomplished with the incorporation of the actual gas temperature measured from plasma OES and is applied to diagnose the 760 Torr nitrogen plasma. Details of this technique are presented in Sec. III.

II. THEORY

A. Millimeter wave interferometry

1. Propagation of millimeter waves in plasma and plasma interferometry

Following the analysis of Heald and Wharton,²⁰ we can obtain the phase and attenuation constants of the plasma as^{10,20}

$$\beta_p = \frac{\omega}{c} \left\{ \frac{1}{2} \left(1 - \frac{\omega_p^2}{\omega^2 + \nu^2} \right) + \frac{1}{2} \left[\left(1 - \frac{\omega_p^2}{\omega^2 + \nu^2} \right)^2 + \left(\frac{\omega_p^2 \nu}{\omega^2 + \nu^2} \right)^2 \right]^{1/2} \right\}^{1/2}, \quad (1)$$

$$\alpha_p = \frac{\omega}{c} \left\{ -\frac{1}{2} \left(1 - \frac{\omega_p^2}{\omega^2 + \nu^2} \right) + \frac{1}{2} \left[\left(1 - \frac{\omega_p^2}{\omega^2 + \nu^2} \right)^2 + \left(\frac{\omega_p^2 \nu}{\omega^2 + \nu^2} \right)^2 \right]^{1/2} \right\}^{1/2}, \quad (2)$$

where ω is the frequency of the electromagnetic wave, c is the speed of light in free space, and the electron plasma frequency is $\omega_p = (n_e e^2 / \epsilon_0 m)^{1/2}$ rad/s.

The objective of our plasma interferometry is to accurately diagnose the line-averaged ν and n_e during the entire plasma pulse. A new approach has been developed and employed to evaluate the plasma characteristics ν , ω_p , n_e , and T_e , based on millimeter wave interferometry.¹⁹ When we launch a plane wave through the plasma, the phase constant β_p and attenuation constant α_p of the wave are given in Eqs. (1) and (2).^{12,20} These expressions can be inverted so that ν and ω_p can be written in terms of the experimentally measured values β_p and α_p ,¹⁹

$$\nu = 2 \left(\frac{c^2}{\omega} \right) \left[\frac{\alpha_p \beta_p}{1 - \frac{c^2}{\omega^2} (\beta_p^2 - \alpha_p^2)} \right], \quad (3)$$

$$\omega_p = \left\{ \left[1 - \frac{c^2}{\omega^2} (\beta_p^2 - \alpha_p^2) \right] \times \left[\omega^2 + 4 \left(\frac{c^4}{\omega^2} \right) \left(\frac{\alpha_p \beta_p}{1 - \frac{c^2}{\omega^2} (\beta_p^2 - \alpha_p^2)} \right)^2 \right] \right\}^{1/2}. \quad (4)$$

Both ν and ω_p are local characteristics of the plasma and are functions of space at any given time. They can therefore be written as $\nu(z, r, \theta, t)$ and $\omega_p(z, r, \theta, t)$, where we use the cylindrical coordinates due to chamber geometry. There exists radial as well as axial profiles for n_e and ν . Note that since β_p and α_p are determined by ν and ω_p , they are local values and therefore also have a spatial variation. However, the interferometry method measures the phase shift and attenuation as an integration over the entire wave path,

$$\Delta\varphi = \int_0^d (\beta_0 - \beta_p) dx, \quad (5)$$

$$A = A_0 e^{\int_0^d (\alpha_0 - \alpha_p) dx}. \quad (6)$$

This is due to the fact that the 105 GHz millimeter wave beam is launched through the entire plasma column and experiences phase shift and attenuation as an integration along the path of propagation (in other words, this is a line-of-sight diagnostic technique). Here, a_0 is the attenuation constant of air ($a_0 \approx 0$), β_0 is the phase constant of free space, d is the inner diameter of the plasma chamber, and x is the integra-

tion variable. $\Delta\varphi$ is the phase shift, A_0 is the initial amplitude, and A is the amplitude of the microwave after attenuation by the plasma.

The transmitting horn antenna of the 105 GHz millimeter wave interferometer is placed 4.5 cm away from the center of the cylindrical plasma so that the plasma is in the far zone of the antenna. At this distance, the transverse width of the millimeter wave beam is approximately 2 cm which is comparable to the radius of the plasma. Because the spatial resolution of millimeter wave interferometry is limited by this beam width, it is impractical to measure the radial profile of ν and n_e in the 5-cm-diameter atmospheric-pressure plasma using Abel inversion. We therefore utilize the line-averaged descriptions of n_e and ν . This has been proven valid by comparing the electron density obtained using the interferometer to Langmuir probe measurements.¹⁹ This is a simplification made necessary by the limitation of the diagnostic method. As a result, the integrations in Eqs. (5) and (6) can be simplified into multiplications as follows^{12,19,22} since the line-averaged β_p and α_p are no longer functions of the radius coordinate r :

$$\Delta\varphi = (\beta_0 - \beta_p)d, \quad (7)$$

$$A = A_0 e^{-\alpha_p d}. \quad (8)$$

In addition to the above simplification, to further facilitate the analysis, we assume a one dimensional (1D) plasma slab model. The plasma is assumed to be infinite in the direction transverse to the microwave propagation and has thickness $d=5$ cm along the direction of propagation. The 1D plasma slab model is justified because the 105 GHz millimeter wave beam bending due to the cylindrical cross section of the plasma at these densities is negligible. At $n_e=10^{10-13}$ cm⁻³, the Lorentz plasma dielectric constant,

$$\varepsilon_r = \left(1 - \frac{\omega_p^2}{\nu^2 + \omega^2}\right) - j \frac{\nu}{\omega} \left(\frac{\omega_p^2}{\nu^2 + \omega^2}\right), \quad (9)$$

is very close to unity at 105 GHz ($\varepsilon_r \approx 1$ for $n_e=10^{10}$ cm⁻³, $\varepsilon_r \approx 0.96 - j 0.037$ for $n_e=10^{13}$ cm⁻³). So the plasma is almost transparent to the millimeter wave with slightly altered propagation constant.²⁰ Therefore, the amplitude drop detected by the receiving horn is almost purely due to plasma attenuation [Eq. (9)], not geometric beam bending. However, when the plasma density is sufficiently high ($n_e > 10^{13}$ cm⁻³), beam bending needs to be taken into account when using interferometry at 105 GHz.

The plasma frequency is related to n_e (in cm⁻³) by

$$\omega_p = 2\pi \times 8.98 \times 10^3 \sqrt{n_e} \quad (10)$$

so we can calculate the line averaged n_e from ω_p .

In summary, we first experimentally measure the total phase shift $\Delta\varphi$ and relative attenuation A/A_0 using the millimeter wave interferometer, then use Eqs. (7) and (8) to calculate the β_p and α_p values and then calculate the line-average plasma characteristics ν , ω_p , and n_e from the calculated β_p and α_p values using Eqs. (3), (4), and (10).

2. Evaluation of electron temperature using millimeter wave interferometry

The total electron-neutral collision frequency is given by^{23,24}

$$\nu = \sigma n_n \bar{v}, \quad (11)$$

in which σ is the total electron collisional cross section between electrons and neutrals and \bar{v} is the scalar average velocity of the electrons. Note that the total cross section σ is a function of T_e . The electron energy E_{eav} is $3/2 k_B T_e$, where k_B is the Boltzmann constant. The curves illustrating the $\sigma(T_e)$ relation for various gases are summarized by Shkarofsky²⁵ and more recently by Zecca.²⁶ Although the cross sections of electron-electron and electron-ion collisions (σ_{ee}, σ_{ei}) are substantial, these collisional processes are negligible compared to electron-neutral processes in our low-fractional-ionization air and nitrogen plasmas ($\nu_{\text{en}} \gg \nu_{ee}, \nu_{ei}$, and $\nu \approx \nu_{\text{en}}$). Therefore in our analysis we use the electron-neutral collisional cross section as the total electron collisional cross section. The scalar average electron velocity \bar{v} is related to the electron temperature T_e by the following relation if we assume a three-dimensional Maxwellian velocity distribution for the electrons,²³

$$\bar{v} = \left(\frac{8k_B T_e}{\pi m_e}\right)^{1/2}. \quad (12)$$

Eliminating \bar{v} , we can combine Eqs. (11) and (12) to write

$$k_B T_e = \frac{\pi m_e}{8} \left[\frac{\nu}{\sigma(T_e) n_n}\right]^2. \quad (13)$$

Since T_e is the only unknown and it is present on both sides of the equation, Eq. (13) can be iteratively solved for the line averaged T_e with ν obtained using our millimeter wave interferometer diagnostic and $\sigma(T_e)$ as tabulated by Zecca.²⁶ In our previous work¹⁹ n_n was obtained using an approximate gas heating rate assumed based on publications on neutral heating in inductively coupled plasmas.²⁷⁻²⁹ In this work, the neutral density n_n is determined based on the ideal gas law for neutrals ($P_n = n_n k_B T_{\text{trans}}$), with T_{trans} obtained based on the neutral gas temperature determined from OES (Sec. II B) and P_n measured experimentally using a fast response pressure gauge. The incorporation of a measured gas temperature and neutral density has greatly improved the accuracy of this electron temperature diagnostic.

B. Plasma spectroscopy

1. Rotational and vibrational temperature diagnostic aided by SPECAIR

SPECAIR is an air plasma optical spectroscopy code developed by Laux *et al.*^{8,15,21} based on NEQAIR by Park.³⁰ The code calculates the OES by determining the populations of the states of the transitions using user-specified electronic, vibrational, and rotational temperatures,^{11,21,31-33} unlike similar codes which use a collisional-radiative model. The modeled transition rates are calculated based on tabulated data for the transitions. From the calculated transition probabilities and populations of radiating species, the line-by-line optical emission intensity is computed for the wavelengths of

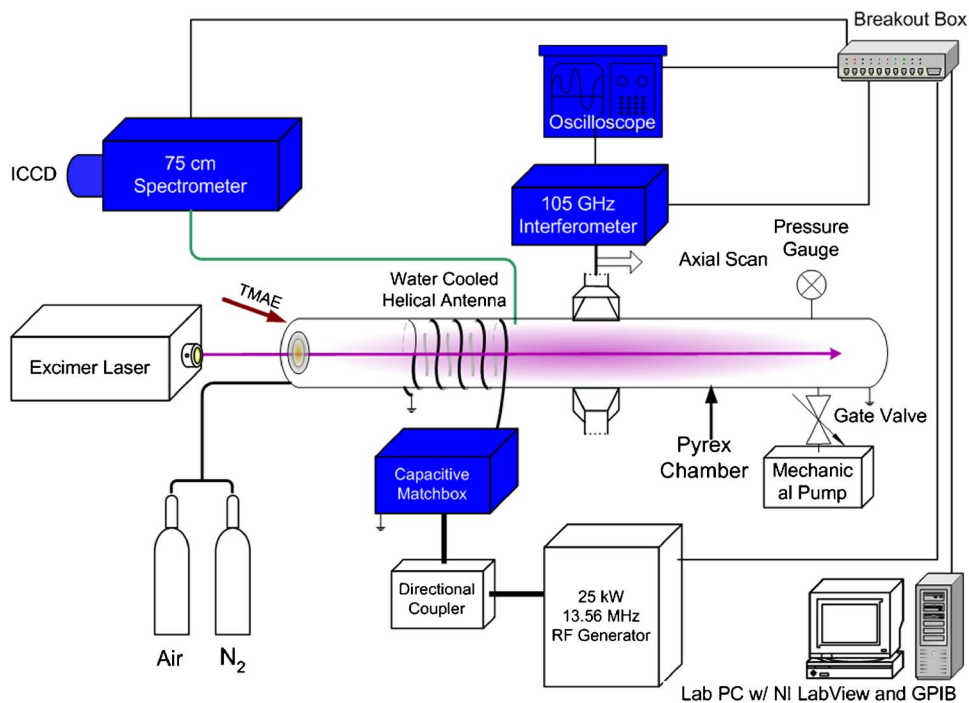


FIG. 1. (Color online) Schematic diagram of the laser initiation and rf-sustained plasma experiment.

the transitions.^{8,11,21} SPECAIR is suitable for nonlocal thermal equilibrium (non-LTE) as well as LTE plasma optical emission studies, making it an ideal software tool for analysis of high-pressure air-constituent plasmas.

T_{trans} is the translational temperature and is often simply referred to as the gas temperature in plasmas. It describes the translational velocity distributions of the N_2 molecules and N_2^+ ions in the nitrogen plasma. The translational temperatures of neutrals and ions are approximately equal in our atmospheric-pressure plasmas due to the high collision rate between these species. $T_{\text{trans}} \approx T_{\text{rot}}$ can be assumed for our atmospheric-pressure plasmas because the rotational relaxation time is fast at atmospheric pressures.^{8,11} Therefore, the OES measurement of T_{rot} is a reliable nonperturbing diagnostic of T_{trans} . Together with the experimentally measured neutral gas pressure P_n , T_{trans} can be used in ideal gas law $P_n = n_n k_B T_{\text{trans}}$ to obtain the neutral density n_n .

The line-of-sight measurement of optical emission from a cylindrical plasma requires Abel inversion to obtain the radial profiles of volumetric emission and therefore to produce radial temperature profiles.^{8,21,34} A computer code has been written to perform the task of Abel inversion and obtain radial emission spectra and thermodynamic properties of the plasma utilizing the SPECAIR code.

III. EXPERIMENTAL SETUP

The experimental setup of the laser-initiated and rf-sustained plasma is shown schematically in Fig. 1. The plasma chamber is a 5 cm inner diameter, 150 cm long Pyrex® tube. The mass flow controllers are located at the gas inlets at the laser window end. The chamber is evacuated to a base pressure of 50 mTorr prior to each experiment. After evacuation, a stable chamber pressure is achieved by fine tuning and balancing the gas input and throttle valves of the mechanical pump to control the gas input and pumping rates.

A thermal gas flow meter (McMillan model 50S) located at the incoming gas pipeline is used to measure the incoming gas flow rate. Typical gas flow rates range from 0.5 to 100 standard liters per minute (SLM). Two microelectromechanical system-based piezo pressure gauges (MKS HPS 902 absolute piezotransducer and 910 dual transducer) are used to monitor the chamber pressure accurately from 10^{-5} to 1000 Torr.

A uniform intensity UV beam of 193 nm wavelength is produced by an excimer laser (Lumonics PulseMaster PM-842) that runs in the ArF (6.4 eV photon energy) mode. The half width of the laser pulse is 20 ± 2 ns, with a 2 ns rise/fall time. The typical working output is 100 mJ with a uniform laser flux output rectangular cross section of 2.8×1.2 cm². The laser beam enters the plasma chamber through a 2.8 cm diameter Suprasil® quartz window (98% transparency at 193 nm wavelength) at the upstream end. Laser energy passing through the UV window is measured using an energy meter (Sciencetech AC 50 UV calorimeter and Astral AD30 laser energy meter). In order to account for the laser attenuation by the UV window, the window is placed in front of the energy meter for this measurement.

The rf circuit diagram is shown in Fig. 2. A 25 kW maximum power 13.56 MHz rf generator (CXH25K, Comdel, Inc.) is used to deliver power to the antenna using an efficient capacitive impedance matching network. The short (20 ns) laser pulse is triggered late during the initial rise of the rf power at the point when the forward rf power is 90% of the power setting, in order to provide the seed plasma for efficient rf coupling at reduced rf power levels. A dual directional coupler (Connecticut Microwave) with 50 dB incident and 40 dB reflected coupling is used to measure the incident and reflected voltages (V_{inc} and V_{ref}) to determine the plasma load impedance $Z_p(t)$ defined at the feed points to the six-turn helical antenna. The rf power is coupled through the helical antenna that excites rf fields in the laser-formed

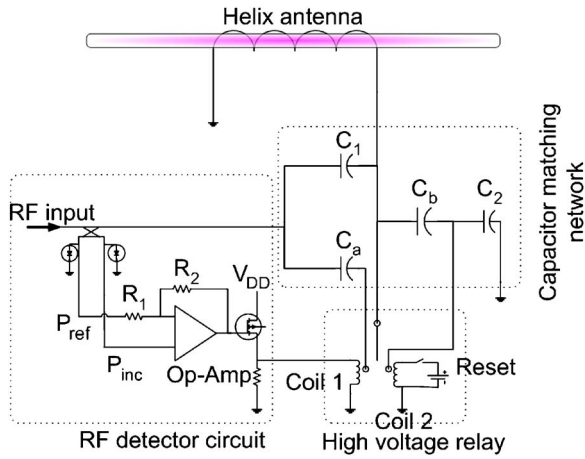


FIG. 2. (Color online) Dynamic rf measurement and matching circuit.

plasma. The water-cooled helical antenna is made of six turns of quarter-inch copper tubing with an axial coil length of 12 cm and an inner diameter of 6 cm, wound over the 5 cm inner diameter chamber. Teflon spacers are inserted between the antenna and Pyrex® chamber to avoid arcing and contact heating of the Pyrex® chamber which is a poor heat conductor. The end of the helical antenna closest to the laser window is grounded to the capacitive matchbox. The high voltage lead of the antenna is toward the pump side of the chamber. rf power is coupled to the capacitive impedance matching network using a 1–5/8 in., 50 Ω semirigid coaxial transmission line (Myat Inc.). Silicone compound is used on high voltage regions in the circuit (especially the antenna feeds) to avoid arcing and current leakage.

A very accurate computer-controlled timing circuit sequences rf turn on and turn off, fast gas injection, laser firing, and data acquisition. First, an initial background gas (air or nitrogen) pressure of 75 Torr with a seed TMAE partial pressure of 15 mTorr is maintained in the chamber with a total air or nitrogen mass flow rate of 0.5 SLM. Because the tube-powered rf generator needs ~ 300 ms to ramp up its power output to 90% of the peak value (4.5 kW), we turn on the generator at $t = -300$ ms. At $t = 0$, the 100 mJ laser pulse is fired through the chamber to create a TMAE seed plasma to assist rf plasma initiation. The electron density of the laser plasma (in the absence of rf) is diagnosed with the millimeter wave interferometry technique and exhibits $n_e > 10^{12}/\text{cm}^3$ with a lifetime of $t \sim 3 \mu\text{s}$, as presented in Fig. 3. The laser-formed TMAE plasma provides a sufficient plasma radiation resistance load ($R_p > 1 \Omega$) for efficient rf coupling through the helical antenna. Also at $t = 0$, an additional valve is switched open to increase the air or nitrogen gas flow to 40 SLM. As a result of this increased gas flow and the plasma neutral heating,¹⁹ the chamber pressure is raised within 0.5 s to 760 Torr. As soon as the 760 Torr pressure is reached, the gas flow is reduced back to 0.5 SLM to balance the pumping rate, and the chamber's end plate is subsequently opened to the ambient air so the plasma is maintained at 760 Torr pressure in the Pyrex® chamber (Fig. 4). Therefore, we are able to create an atmospheric-pressure plasma within 0.5 s and maintain it in a steady state for several seconds. The 500 ms pressure rise from 75 to 760 Torr facilitates the atmospheric

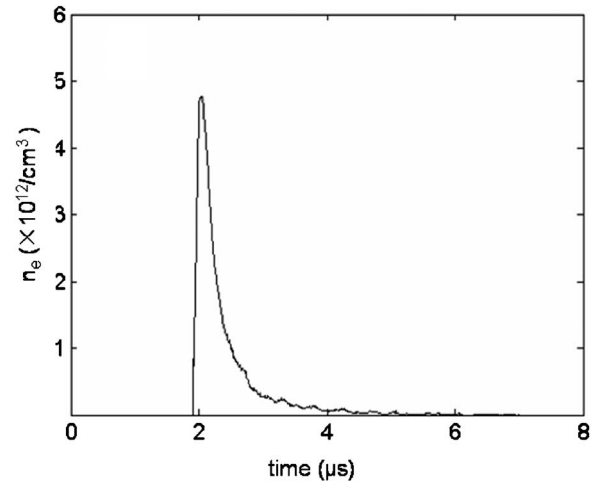


FIG. 3. Electron density of the laser-initiated TMAE seed plasma in 760 Torr nitrogen background.

plasma formation, allows for a smooth helical antenna impedance transition from the vacuum antenna level to the plasma-coupled level, and eliminates the unstable, lower density, filamentary intermediate plasma stage observed in our previous work.¹⁹ The steady-state atmospheric-pressure plasma can be sustained for as long as 5 s. The pulse duration is only limited by the heating of the Pyrex® chamber.

In addition to the timing of the laser, rf, and gas feed, a dynamic matching network is used for optimum coupling of rf power into the plasma. We have shown that when the laser-rf plasma is created and sustained, the plasma impedance will vary from the vacuum antenna impedance $Z_a = R_a + jX_a$ to the plasma impedance $Z_p = R_p + jX_p$.¹⁹ The difference between Z_a and Z_p is significant and poses a challenge to the matching network. An ac transformer model has been used to account for the plasma coupling and plasma impedance variation²⁴ which agrees with our experimental results. This transition exactly coincides with the formation of the large-volume rf-sustained plasma which reaches steady state 2 ms after the laser pulse.

In order to match the varying plasma load impedance, the four capacitors in Fig. 2 are preset following the work of Kelly *et al.*,³⁵

$$C_1 = \frac{R_a/R_0}{\gamma_a \omega_{\text{rf}}}, \quad C_2 = \frac{(X_a - \gamma_a)}{(X_a^2 + R_a^2) \omega_{\text{rf}}}, \quad (14)$$

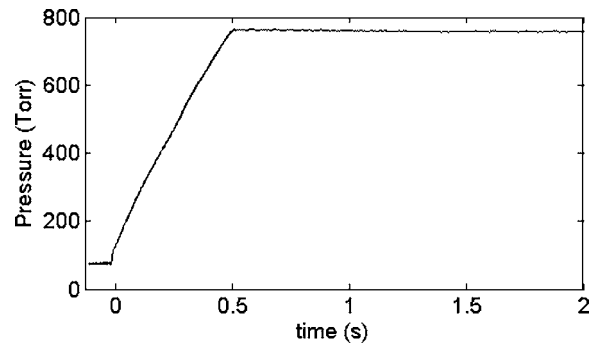


FIG. 4. Controlled gas delivery during a plasma pulse.

$$C_1 + C_a = \frac{R_p/R_0}{\gamma_p \omega_{rf}}, \quad (C_2^{-1} + C_b^{-1})^{-1} = \frac{(X_p - \gamma_p)}{(X_p^2 + R_p^2) \omega_{rf}}, \quad (15)$$

where $\gamma_a = \sqrt{R_a/R_0} \sqrt{X_a^2 + R_a(R_a - R_0)}$ and $\gamma_p = \sqrt{R_p/R_0} \sqrt{X_p^2 + R_p(R_p - R_0)}$,³⁵ so that the vacuum antenna impedance can be matched to the $R_0 = 50 \Omega$ rf network by C_1 and C_2 , and the plasma impedance at a later time can be matched by $C_1 + C_a$ and $(C_2^{-1} + C_b^{-1})^{-1}$.

A control circuit is required so that these two sets of matching networks can be switched when the plasma is formed. To this end, we have designed and utilized a dynamic rf measurement and matching system. This system (Fig. 2) has three major parts. The first is a rf detector circuit that is composed of a dual directional coupler, a pair of rf detectors, an operational amplifier circuit, and a metal oxide semiconductor field effect transistor (MOSFET) amplifier. This circuit detects the incident and reflected rf power levels and compares them at the operational amplifier. The output from the operational amplifier is then amplified by the MOSFET and used to drive the switching relay. The second part of the system is the high-voltage rf relay which is responsible for switching between the two capacitor settings at the output of the rf detector circuit. The switch time of the circuit is 4 ms which is limited by the mechanical rf relay driven by a dc magnet coil. The third part is the capacitor matching network that has two preset capacitor settings as discussed above, so that when the plasma impedance changes from vacuum antenna to plasma loaded antenna impedance, a corresponding setting can be enabled to compensate for the impedance variation.

In a typical experiment, the working procedure of this dynamic matching system is as follows. Before the plasma pulse, the capacitor matching system is set to match the vacuum antenna impedance Z_a (i.e., C_1 and C_2 are set). Then the laser and rf power are enabled to start the plasma. When the large-volume, high-pressure plasma is formed 2 ms after the laser seed plasma, a different plasma impedance Z_p is seen at the antenna load. As a result, the mismatch is detected by the dual directional coupler. This mismatch signal is amplified to produce a large voltage signal (>5 V) that is used to drive the high voltage relay coil 1 and switch the matching network to the settings of $C_1 + C_a$ and $(C_2^{-1} + C_b^{-1})^{-1}$ that are preset to match the premeasured steady-state plasma impedance. In other words, the comparator circuit compares the incident and reflected rf powers. A plasma load impedance variation will manifest itself as a transient in the rf power reflection coefficient. This transient signal is then detected and amplified by the comparator circuit and is used to switch the matching network on a rapid time scale (2 ms) to compensate for the plasma impedance variation. The experimental results of this matching technique are presented in Sec. IV.

Both microwave and optical diagnostics are carried out to analyze the plasmas created. A Quinstar millimeter wave interferometer is used to diagnose electron density and electron collision frequency of the plasma. Plasma optical emission spectra are obtained and analyzed. The full optical bandwidth (300–780 nm) emission of the steady-state plasma is collected by an Ocean Optics ST2000 spectrometer with 10

ms integration time. This spectrometer has a slit function with a full width half maximum (FWHM) of 1 nm. The results are used to identify the radiating species. High-resolution molecular spectroscopy analysis is carried out using an Andor iStar ICCD detector integrated with an Acton SpectraPro 2750 spectrograph system. This system has a near-Lorentzian slit function with a FWHM of 0.2 nm when the grating density is set to 2400 lines/mm. The experimental spectra profiles are compared to the SPECAIR simulation results to determine the rotational and vibrational temperatures of the molecules in the plasma.

IV. EXPERIMENT AND RESULTS

A. Creation of laser-initiated, rf-sustained air and nitrogen plasmas

In order to make the plasma seeding technique effective and efficient, the dynamic plasma matching system discussed in Sec. III is employed to ensure an impedance match when the load impedance varies significantly during the plasma formation. Using the impedance diagnostic we designed,¹⁹ the plasma impedance Z_p is found to be $3.2 + j 121 \Omega$ when the plasma is stabilized ($t = 1.5$ s), while the vacuum antenna impedance Z_a is $0.6 + j 125 \Omega$. According to a transformer coupling model,²⁴ if the inductive mode (H mode) is the plasma coupling mode, the equivalent load impedance measured at the terminals of the helical antenna will have a significantly increased resistance and reduced inductance compared to the vacuum antenna impedance, which is the case for this plasma. The dynamic plasma measurement and matching system discussed in Sec. III ensure a low rf power reflection coefficient ($|\Gamma|^2 < 5\%$) during the entire 760 Torr air plasma pulse, as shown in Fig. 5. The short spike in the reflected power curve exists because the capacitor switching requires 4 ms which is limited by the switching relay, while the plasma formation time is 2 ms. This spike does not affect incident power or plasma formation. Assisted by the approximately 60 cm long laser-initiated seed plasmas,¹² the rf-sustained plasmas are projected approximately 30 cm downstream from the helical antenna. Photographs of the steady-state 760 Torr, 1000 cm³ air, and nitrogen plasmas thus created are shown in Figs. 6 and 7, respectively.

B. Temporal variation of electron density and collision frequency

The electron density and electron collision frequency of the air and nitrogen plasmas measured with the millimeter wave interferometer at 10 cm downstream from the end of the helical antenna are presented in Figs. 8 and 9. Both plasmas approach a steady state 2 ms after they are initiated as suggested by the stable electron density and collision frequency levels shown in Figs. 8 and 9. Similar electron collision frequency levels of 10^{11} Hz are observed in both plasmas. However, the air plasma exhibits a higher electron density level of $3.4 \times 10^{12}/\text{cm}^3$, while a $3.5 \times 10^{11}/\text{cm}^3$ density is observed in the nitrogen plasma. This is partly due to the 21% oxygen present in the air plasma, which has a lower ionization potential than nitrogen. Also at elevated gas temperature ($T_g > 2000$ K), the rate of electron attachment to

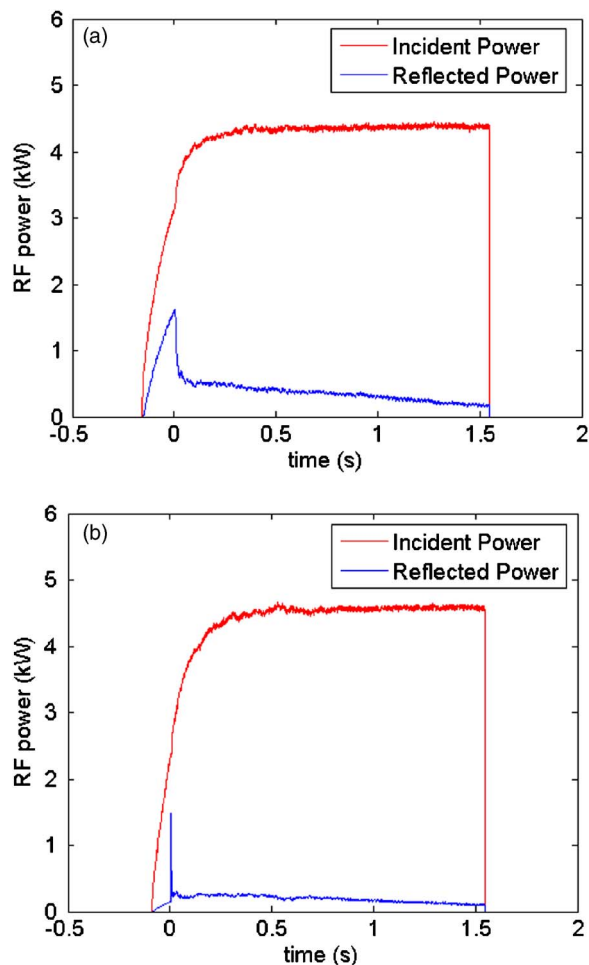


FIG. 5. (Color online) Incident and reflected rf power to the matchbox: (a) original matching circuit; (b) dynamic matching circuit.

oxygen is greatly reduced, while the electron recombination to positive nitrogen ions and electron collisional excitation of nitrogen molecules is very efficient, consuming large amounts of rf power.^{7,9,13} Therefore, given the same laser and rf power density, a significantly higher electron density level can be maintained in air plasmas than in nitrogen-only plasmas at 760 Torr.

C. Spectroscopic and thermodynamic analysis of the atmospheric air and nitrogen plasmas

Both high-resolution plasma emission spectroscopy and full bandwidth (300–780 nm) spectroscopy are utilized to diagnose the plasmas for the emitting species and their ther-

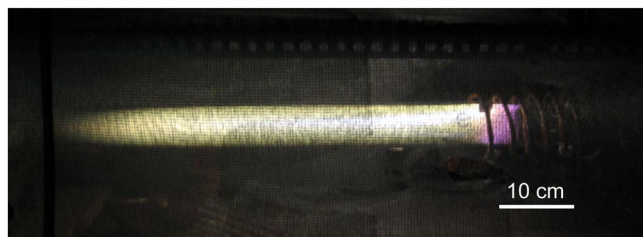


FIG. 6. (Color online) Photograph of 760 Torr air plasma created by 100 mJ laser initiation and 4.5 kW net rf power. The image is taken at $t \approx 1.5$ s after initiation.

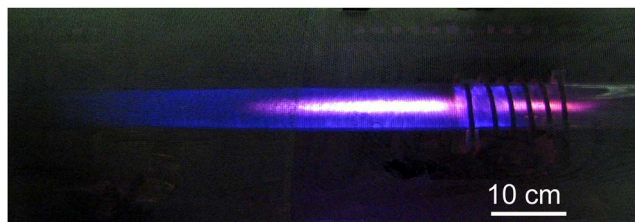


FIG. 7. (Color online) Photograph of 760 Torr nitrogen plasma created by 100 mJ laser initiation and 4.5 kW net rf power. The image is taken at $t \approx 1.5$ s after initiation. A visually distinct 2.5 cm diameter center region exists with significantly more optical emission than the outer region of the plasma. Optical diagnostics are focused on the 2.5 cm diameter center region where strong and consistent emission is observed.

modynamic characteristics. All high-resolution spectral results are Abel inverted to obtain the radial profiles of volumetric emission and, therefore, to produce radial temperature profiles. All spectra are acquired 10 cm downstream from the end of the helical antenna after the plasma is sufficiently stabilized ($t > 1.5$ s after plasma initiation) with an integration time of 10 ms.

The 760 Torr laser-initiated, rf-sustained air plasma exhibits a complex spectrum over the entire detectable range of 290–780 nm (Fig. 10). Overlapped O_2 Schumann–Runge and $N_2^+(1-)$ transitions are prominent in the shorter wavelength range (< 500 nm), while $N_2(1+)$ is the most prominent feature at the long wavelengths. This is because the O_2

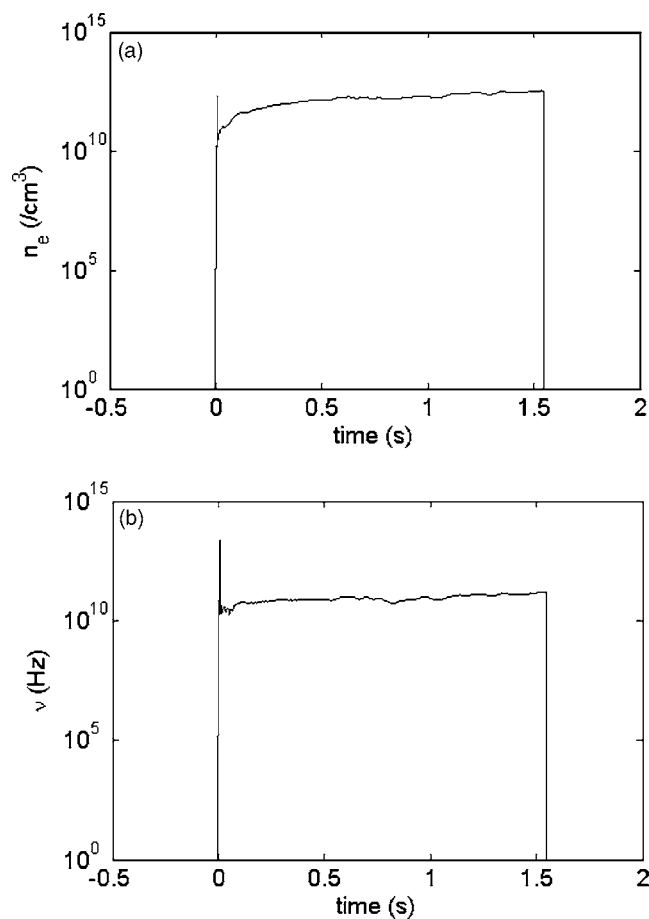


FIG. 8. Temporal variation of plasma density and collision frequency in 760 Torr air plasma.

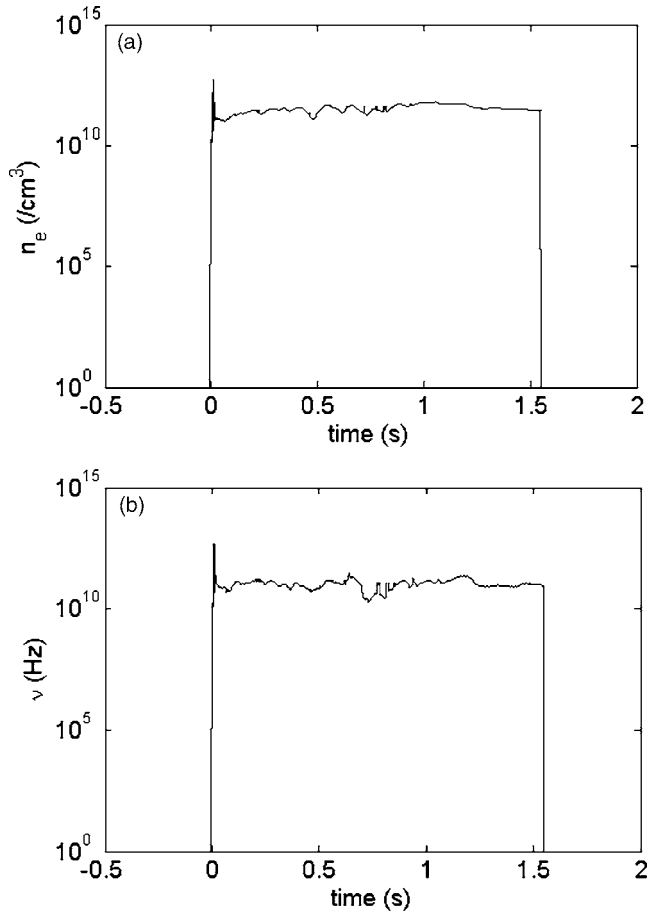


FIG. 9. Temporal variation of plasma density and collision frequency in 760 Torr nitrogen plasma.

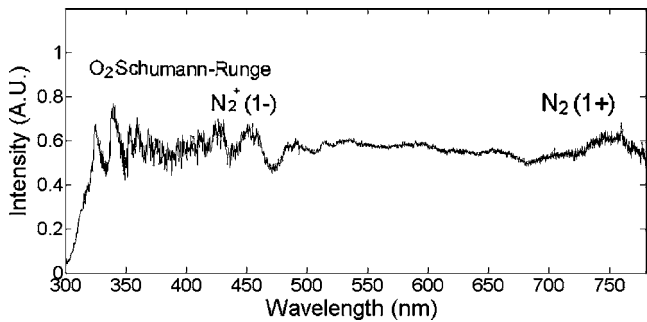


FIG. 10. Full bandwidth optical emission spectrum of 760 Torr air plasma.

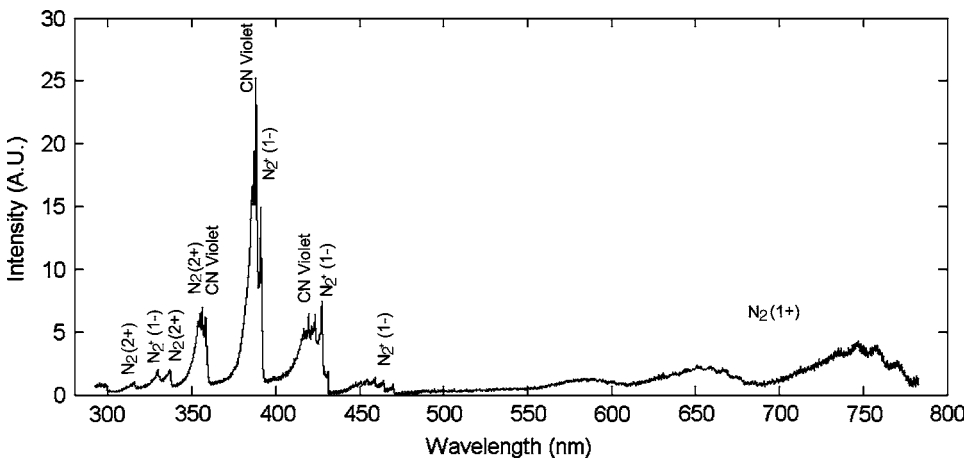


FIG. 11. Full bandwidth optical emission spectrum of 760 Torr nitrogen plasma.

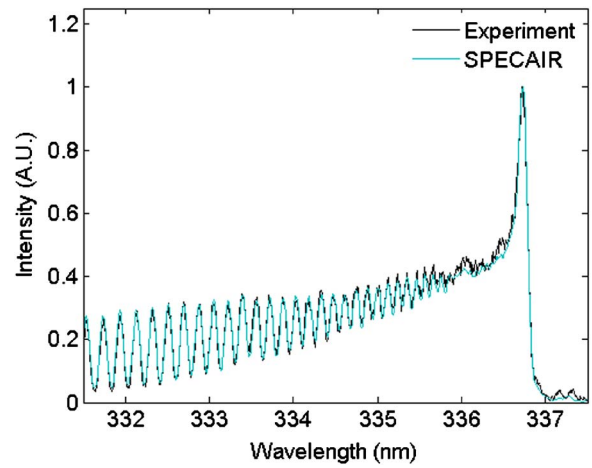


FIG. 12. (Color online) Emission spectra of $N_2(2+) \Delta\nu=0$ band.

Schumann–Runge and $N_2^+(1-)$ transitions dominate with higher neutral temperature levels (3000–5000 K) (Ref. 8) which our plasmas exhibit. The overlap between O_2 Schumann–Runge and other possible transitions in the shorter wavelength region makes further analysis of thermodynamics of these air plasma species impractical using this method.

Without the O_2 Schumann–Runge transitions present, the full bandwidth optical emission spectrum of 760 Torr nitrogen-only plasma is readily diagnosed with $N_2(2+)$, CN violet, $N_2^+(1-)$, and $N_2(1+)$ transitions aided by SPECAIR (Ref. 8) (Fig. 11). The reason why the CN violet lines are observed is because TMAE is used as the seed plasma. The organic compound TMAE ($C_{10}N_4H_{16}$) can be decomposed into CN products in the plasma. Additionally, TMAE gives rise to smaller-molecule, carbon-rich residuals on the Pyrex® chamber wall, which form CN with nitrogen and re-enter the plasma in gaseous state when heated by the neutrals and plasma bombardment of the Pyrex® chamber wall.

High-resolution spectroscopy is used to analyze the plasma emission from $N_2(2+)$ and $N_2^+(1-)$ transitions. Various transitions [$N_2(2+) \Delta\nu=0$ in Fig. 12, $N_2^+(1-) \Delta\nu=-1$ and $\Delta\nu=-2$ in Fig. 13] are resolved from interfering CN transitions and used to obtain T_{rot} and T_{vib} . Due to the CN lines in close proximity, the $\Delta\nu=-1$ transition is not fully

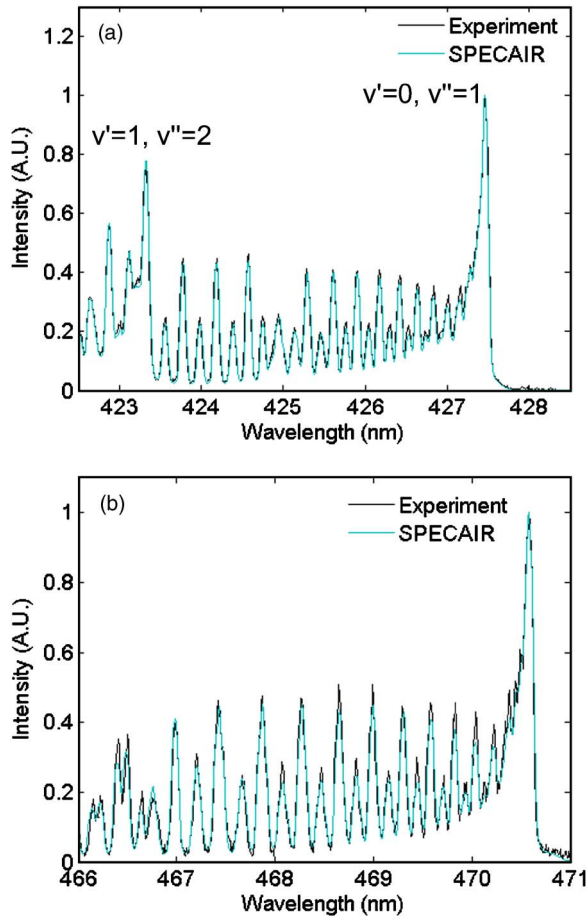


FIG. 13. (Color online) Emission spectra of $N_2^+(1-)$ transitions: (a) $\Delta\nu=-1$ and (b) $\Delta\nu=-2$.

observable. As a result, only the (0,1) and (1,2) bands are seen for this transition. The experimental spectra are fitted with the SPECAIR code-simulated spectra as shown in Figs. 12 and 13.

T_{rot} values are obtained by fitting the SPECAIR code-generated spectral profiles with the experimental ones.^{8,21,30} We have obtained excellent fit between the SPECAIR code-simulated spectra and experimental spectra. The rotational temperatures are 4400 ± 50 K from $N_2(2+) \Delta\nu=0$, 4600 ± 100 K from $N_2^+(1-) \Delta\nu=-1$, and 4600 ± 100 K from $N_2^+(1-) \Delta\nu=-2$ (Figs. 12 and 13). Assuming $T_{\text{trans}} \approx T_{\text{rot}}$ for nitrogen,^{8,11} the translational temperature of N_2 molecules is 4400 ± 50 K.

The T_{vib} value of N_2^+ is obtained from the relative intensities of vibrational bands. T_{vib} is found to be 4500 ± 100 K from the relative intensities of (0,1) and (1,2) vibrational bands of the $N_2^+(1-)$ transition [Fig. 13(a)]. The SPECAIR code simulation has an accuracy of ± 50 K for $N_2(2+)$ and ± 100 K for $N_2^+(1-)$ transitions.⁸ Within the accuracy of the experiment, T_{rot} is comparable to T_{vib} as obtained from $N_2^+(1-) \Delta\nu=-1$ bands.

The radial profile of the plasma temperatures is obtained by fitting the Abel-inverted emission lines from the series of radial positions with code-predicted results and shown in Fig. 14. Notice that the 760 Torr nitrogen plasma shows a 2.5 cm diameter central region with significantly stronger optical

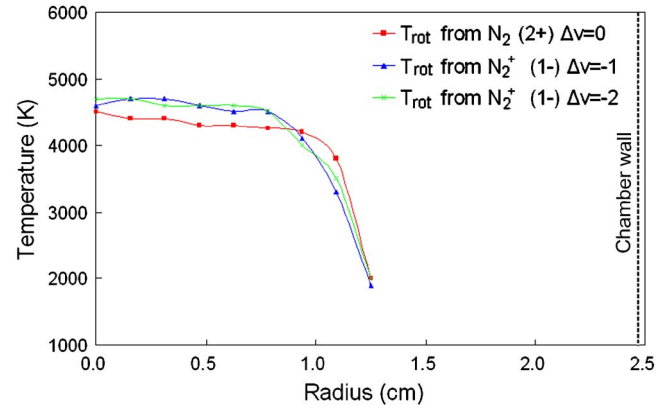


FIG. 14. (Color online) Radial temperature profiles of 760 Torr nitrogen plasma: (a) temperatures from $N_2(2+)$ transitions; (b) temperatures from $N_2^+(1-)$ transitions.

emission than the outer region of the plasma (Fig. 7). Consequently the lateral line-of-sight optical emission is only measured radially from 0 to 1.25 cm from the center of the plasma, therefore the Abel-inverted spectra and radial temperature data are available only for this range of radii. Temperature data cannot be obtained at radii larger than 1.25 cm since the emission intensity is too low compared to the central region.

Based on the millimeter wave interferometry measurement, the electron collision frequency is 1.0×10^{11} Hz in the 760 Torr nitrogen plasma 1.5 s after the initiation when the plasma is in steady state (Fig. 9). Meanwhile, for the same steady-state plasma, the translational neutral molecular temperature T_{trans} is 4400 ± 50 K as derived from $N_2(2+) \Delta\nu=0$ transition. We can therefore use Eq. (13) and the tabulated total collision cross-section data of nitrogen²⁶ to iteratively solve for the electron temperature T_e .¹⁹ The T_e value is found to be 0.75 ± 0.01 eV or 8700 ± 100 K.

V. CONCLUSIONS AND DISCUSSION

The laser-initiated and rf-sustained plasma generation method has been substantially improved over our previous work.¹⁹ Improvements to the experiment include rf mismatch detection, a new dynamic tuning system, and a fast gas delivery scheme. As a result, we have been able to create large-volume (≥ 1000 cm³), atmospheric pressure, steady-state air, and nitrogen plasmas within 500 ms and sustain them for long durations of up to 5 s limited only by the neutral heating of the Pyrex® chamber, with a sustaining rf power requirement of 5 W/cm³. In this method, although a high-power pulsed excimer laser beam is utilized to initiate the plasma, the overall power budget is still approximately 5 W/cm³. This is because the 100 mJ laser pulse is only 20 ns, and it occurs once at the beginning of the plasma, whereas the plasma is sustained up to more than 2 s, limited only by heating of the Pyrex chamber. Only 100 mJ of total laser energy is used to initiate the plasma, while over 10 kJ of rf power is put into the plasma to sustain it for over 2 s. Even when the relatively low efficiency of conversion of wall power to beam power for the laser is taken into account ($\sim 1\%$), the energy supplied by the laser is only 0.1% of that

supplied by rf generator. In situations where more aggressive cooling of the chamber is performed, the rf plasma could be sustained for much longer periods of time, for which the initial laser energy would be a further diminishing portion of the total power budget for plasma creation.

The electron density and collision frequency are diagnosed using 105 GHz millimeter wave interferometry. The air plasma exhibits a higher line-average electron density level of $3.4 \times 10^{12}/\text{cm}^3$, while a $3.5 \times 10^{11}/\text{cm}^3$ density is observed for the nitrogen-only plasma. This is expected due to the lower oxygen ionization energy level compared to nitrogen. Electron collision frequency levels of 10^{11} Hz are determined in both the air and nitrogen-only plasmas. The low power density needed to produce our laser laser-initiated, rf-sustained large-volume plasma is aided by the laser-TMAE seeding technique, relatively high gas temperature, and moderate electron density.

Full bandwidth optical emission spectra of both air and nitrogen plasmas are obtained. O_2 Schumann–Runge, $\text{N}_2^+(1-)$, and $\text{N}_2(1+)$ transitions dominate the 760 Torr air plasma emission spectrum. The $\text{N}_2(2+)$, CN violet, $\text{N}_2^+(1-)$, and $\text{N}_2(1+)$ transitions are the primary optical radiation characteristics of the 760 Torr nitrogen plasma. For the 760 Torr nitrogen plasma, high-resolution spectroscopic tools are used to resolve the $\text{N}_2(2+)$ and $\text{N}_2(1+)$ lines from the CN violet lines. By fitting the SPECAIR code-generated spectra with experimental spectra, rotational and vibrational temperatures of $4400\text{--}4600 \pm 100$ K are obtained. Because the rotation-to-translation relaxation is fast at atmospheric pressure, $T_{\text{trans}} \approx T_{\text{rot}}$ can be assumed.^{8,11} By using the relation between electron collision frequency, electron temperature, and translational neutral temperature [Eq. (13)], we found that T_e is 0.75 ± 0.01 eV or 8700 ± 100 K using an electron-neutral collision cross-section area σ of 10.3×10^{-16} cm² based on tabulated nitrogen cross-section data by Zecca.²⁶

As low-mass charged particles, mobile electrons readily receive energy from the incident rf field (Eqs. (1)–(4)). The electrons in turn transfer their kinetic energy to the vibrational excitation of molecules through collisions. In the 760 Torr air and nitrogen plasmas, this transfer is fast because the electron energy (0.75 eV) resonates readily with the vibrational energy levels of the oxygen and nitrogen molecules.^{8,11,36} The rapid vibrational-translational relaxation process then causes T_{trans} and T_{rot} to become almost equal to T_{vib} .^{8,11,36} This explains why $T_e > T_{\text{vib}} \approx T_{\text{rot}} (=T_{\text{trans}})$ is observed in our 760 Torr nitrogen plasma. Because T_e is considerably higher than the vibrational, rotational, and translational temperatures of the heavier particles (N_2 and N_2^+), the atmospheric-pressure 1000 cm³ volume nitrogen plasma created by the laser-initiation and rf-sustainment technique deviates significantly from LTE.

ACKNOWLEDGMENTS

This research was supported by USAFOSR Grant No. FA9550-06-1-0172 and DURIP Equipment Grant No. FA9550-06-1-0285. We thank D. Staack and Professor A. A. Fridman of Drexel Plasma Institute for many helpful discussions.

- ¹P. Tsai, L. Wadsoworth, and J. R. Roth, *Text. Res. J.* **67**, 359 (1997).
- ²K. Kelly-Wintenberg, T. C. Montie, C. Brickman, J. R. Roth, A. K. Carr, K. Sorge, L. C. Wadsworth, and P. P. Y. Tsai, *J. Ind. Microbiol. Biotechnol.* **20**, 69 (1998).
- ³K. L. Kelly, J. E. Scharer, G. Ding, M. Bettenhausen, and S. P. Kuo, *J. Appl. Phys.* **85**, 63 (1999).
- ⁴R. J. Vidmar, *IEEE Trans. Plasma Sci.* **18**, 733 (1990).
- ⁵R. J. Roth, 44th Annual Meeting of the Division of Plasma of the American Physical Society, 2002 (unpublished), Abstract No. C12.006.
- ⁶M. Laroussi, *Int. J. Infrared Millim. Waves* **17**, 2215 (1996).
- ⁷R. J. Vidmar and K. R. Stalder, Proceedings of the AIAA, 2003 (unpublished), pp. 1–8.
- ⁸C. O. Laux, T. G. Spencer, C. H. Kruger, and R. N. Zare, *Plasma Sources Sci. Technol.* **12**, 125 (2003).
- ⁹I. V. Adamovich, A. P. C. J. W. Rich, and S. A. Zhdanok, *Analysis of the Power Budget and Stability of High-Pressure Nonequilibrium Air Plasmas*, AIAA Plasma Dynamics and Lasers Conference, 31st, Denver, CO, June 19–22, 2000, pp. 1–19.
- ¹⁰Y. P. Raizer, *Gas Discharge Physics* (Springer-Verlag, Berlin, 1991).
- ¹¹D. Staack, B. Farouk, A. F. Gutsol, and A. A. Fridman, *Plasma Sources Sci. Technol.* **15**, 818 (2006).
- ¹²K. Akhtar, J. E. Scharer, S. Tysk, and C. M. Denning, *IEEE Trans. Plasma Sci.* **32**, 813 (2004).
- ¹³S. O. Macheret, M. N. Shneider, and R. B. Miles, *Modeling of Plasma Generation in Repetitive Ultra-Short DC, Microwave, and Laser Pulses*, AIAA Plasma Dynamics and Lasers Conference, 32nd, and Weakly Ionized Gases Workshop, 4th, Anaheim, CA, June 11–14, CA, 2001, pp. 1–29.
- ¹⁴C. H. Kruger, T. G. Owano, and C. O. Laux, *IEEE Trans. Plasma Sci.* **25**, 1042 (1997).
- ¹⁵K. H. Becker, U. Kogelschatz, K. H. Schoenbach, and R. J. Barker, *Nonequilibrium Air Plasmas at Atmospheric Pressure* (Taylor & Francis, London, 2005).
- ¹⁶C. H. Kruger, C. O. Laux, L. Yu, D. M. Packan, and L. Pierrot, *Pure Appl. Chem.* **74**, 337 (2002).
- ¹⁷G. Ding, J. E. Scharer, and K. Kelly, *Phys. Plasmas* **8**, 334 (2001).
- ¹⁸K. L. Kelly, J. E. Scharer, E. S. Paller, and G. Ding, *J. Appl. Phys.* **92**, 698 (2002).
- ¹⁹S. Luo, J. E. Scharer, M. Thiyagarajan, and C. M. Denning, *IEEE Trans. Plasma Sci.* **34**, 2637 (2006).
- ²⁰M. A. Heald and C. B. Wharton, *Plasma Diagnostics with Microwaves* (Wiley, New York, 1965).
- ²¹C. O. Laux, PhD thesis, Stanford University, 1993.
- ²²K. Akhtar, J. E. Scharer, S. Tysk, and E. Kho, *Rev. Sci. Instrum.* **74**, 996 (2003).
- ²³F. F. Chen, *Introduction to Plasma Physics and Controlled Fusion*, 2nd ed. (Plenum, New York, 1984).
- ²⁴M. A. Lieberman and A. J. Lichtenberg, *Principles of Plasma Discharges and Materials Processing*, 2nd ed. (Wiley, New York, 2005).
- ²⁵P. Shkarofsky, T. W. Johnston, and M. P. Bachynski, *The Particle Kinetics of Plasmas* (Addison-Wesley, Reading, MA, 1966).
- ²⁶A. Zecca, G. P. Karwasz, and R. S. Brusa, *Riv. Nuovo Cimento* **19**, 1–146 (1996).
- ²⁷W. Finkelburg and H. Maecker, *Handbuch Der Physik* (Springer-Verlag, Berlin, 1956), Vol. XXII.
- ²⁸D. B. Hash, D. Bose, M. V. V. S. Rao, B. A. Cruden, M. Meyyappan, and S. P. Sharma, *J. Appl. Phys.* **90**, 2148 (2001).
- ²⁹M. W. Kiehlich and D. B. Graves, *J. Appl. Phys.* **91**, 3539 (2002).
- ³⁰C. Park, Nonequilibrium Air Radiation (NEQAIR) Program: User's Manual, NASA-Ames Research Center, Moffett Field, CA, Technical Memorandum, 1985.
- ³¹J. H. Kim, Y. H. Choi, and Y. S. Hwang, *Phys. Plasmas* **13**, 093501 (2006).
- ³²H. R. Griem, *Plasma Spectroscopy* (McGraw-Hill, New York, 1964).
- ³³H. R. Griem, *Principles of Plasma Spectroscopy* (Cambridge University Press, Cambridge, 1997).
- ³⁴I. H. Hutchinson, *Principles of Plasma Diagnostics*, 2nd ed. (Cambridge University Press, Cambridge, 2005).
- ³⁵K. L. Kelly, PhD thesis, University of Wisconsin-Madison, 2001.
- ³⁶A. Fridman and L. A. Kennedy, *Plasma Physics and Engineering*, 1st ed. (Taylor & Francis, New York, 2004).